Enhanced potassium storage capability of two-dimensional transition metal chalcogenides enabled by a collective strategy

Yuhan Wu,[†] Qingcheng Zhang,[‡] Yang Xu,[†,§] Rui Xu,[†] Lei Li,[‖] Yueliang Li,[⊥] Chenglin Zhang,[†] Huaping Zhao,[†] Shun Wang,[*,‡] Ute Kaiser,[⊥] and Yong Lei[*,†]

[†]Fachgebiet Angewandte Nanophysik, Institut für Physik & ZMN MacroNano (ZIK), Technische Universität Ilmenau, Ilmenau 98693, Germany

[‡]College of Chemistry and Materials Engineering, Wenzhou University, Zhejiang 325035, China

[§]Department of Chemistry, University College London, London WC1H 0AJ, UK

[‖]College of Chemical Engineering, Zhejiang University of Technology, Hangzhou 310014, China

[⊥]Central Facility for Electron Microscopy, Electron Microscopy Group of Materials Science, Ulm University, Ulm 89081, Germany

Keywords: $MoSe_2$, multiwall carbon nanotubes, crystallinity, anode, high-rate capability, potassium storage

Abstract

Potassium-ion batteries (PIBs) have been considered as a promising alternative to lithium-ion batteries due to their merits of high safety and low cost. Two-dimensional transition metal chalcogenides (2D TMCs) with high theoretical specific capacities and unique layered structures have been proven to be amenable materials for PIB anodes. However, some intrinsic properties including severe stacking and unsatisfactory conductivity restrict their electrochemical performance, especially rate capability. Herein, we prepared a heterostructure of high-crystallized ultrathin $MoSe_2$ nanosheets coated multiwall carbon nanotubes and investigated its electrochemical properties with a view to demonstrating the enhancement of a collective strategy for K storage of 2D TMCs. In such a heterostructure, the constructive contribution of CNTs not only suppresses the restacking of $MoSe_2$ nanosheets but also accelerates electron transport. Meanwhile, the $MoSe_2$ nanosheets loaded on CNTs exhibit an ultrathin feature, which can expose plentiful active sites for the electrochemical reaction and shorten K^+ diffusion length. Therefore, the synergistic effect between ultrathin $MoSe_2$ and CNTs endows the resulting nanocomposite with superior structural and electrochemical properties. Additionally, the high crystallinity of the $MoSe_2$ nanosheets further promotes the improvement of electrochemical performance. The composite electrode delivers high rate capacities of 209.7 and 186.1 mA h g^{-1} at high current densities of 5.0 and 10.0 A g^{-1}, respectively.

1. Introduction

Since lithium-ion batteries (LIBs) were commercialized by the Sony Corporation in 1991, this kind of rechargeable battery has rapidly dominated the market of electrochemical energy storage.[1-4] However, the scarcity and uneven distribution of lithium sources in the earth's crust overshadow the future of LIBs.[5-8] In recent years, potassium-ion batteries (PIBs) as a promising alternative to LIBs have come into the spotlight because of their distinguished features, such as the similar redox potential of K/K^+ to that of Li/Li^+, the greater abundance and accessibility of potassium resources, and the higher ion-insertion potential.[6, 9-14] Until now, a variety of materials have been explored as PIB anodes, among which two-dimensional transition metal chalcogenides (2D TMCs) have been considered a potential option because of their high theoretical capacities and unique structural properties.[5, 6] Unfortunately, 2D TMCs are largely restricted by the issues of easy stacking and relatively low electronic conductivity, resulting in rapid capacity fading and insufficient electrochemical performance.[15, 16]

To circumvent the aforementioned problems and meanwhile to improve electrochemical performance, structured design and carbon modification have been widely adopted. Structured design can endow 2D TMCs with a few advantages: (I) the severe aggregation of 2D nanosheets can be prevented, thus exposing plentiful active sites for electrochemical reactions; (II) ion and electron diffusion pathways are shortened effectively; (III) the strain of volume change during discharge-charge processes is alleviated to a certain extent.[17-19] With regard to hybridizing with carbon materials, it is no doubt that the problem of the inferior conductivity can be relieved, which is in favor of enhancing rate capability.[15, 20-23] Besides, characteristic properties originated from carbon materials can be integrated into the resulting composite.[21, 22, 24, 25] For example, porous carbon with excellent adsorption enables electrolytes to adequately infiltrate into active materials.[26] Additionally, to achieve a further enhancement of K storage capability, the crystallinity of 2D TMCs that directly decides their electrochemical performance in different mechanism-dominated reactions should attract more attention.[27] Although previous studies obtained encouraging results by using various material engineering technologies, it is still necessary to explore the relationship between the material themselves and their electrochemical properties with a view to pursuing further improvement. Based on these recognitions, a collective strategy that combines structured design, carbon modification, and crystallinity regulation appears to be a feasible route to optimize the energy storage capability of 2D TMCs in PIBs.

In this work, $MoSe_2$, a flagship member of the 2D TMCs' family, is chosen as a demonstrator because of its relatively large interlayer spacing and narrow bandgap; 1D multiwall carbon nanotubes (CNTs) with excellent mechanical robustness, superior chemical stability, and high electronic conductivity are engaged as a scaffold for planting high-crystallized 2D nanostructured $MoSe_2$. The synthesized nanocomposite is endowed with better structural and electrochemical properties, thereby realizing enhanced electrochemical performance in a synergistic manner. Firstly, the severe aggregation of $MoSe_2$ nanosheets is effectively inhibited, exhibiting an ultrathin feature. Secondly, the ultrathin $MoSe_2$ nanosheets provide a large surface area to electrochemical reactions and short percolation pathways for electrolytes. Thirdly, electron transport is accelerated benefiting from the good conductivity of CNTs. Last but not the least, the high crystallinity of $MoSe_2$ nanosheets makes an important contribution to K storage at high rates. All of these advantages collaboratively promote the electrochemical reaction to a considerable degree. Serving as an anode in PIBs, the composite electrode exhibits high capacitive contributions at realatively low scan rates and thus delivers competitive rate capability (209.7 and 186.1 mA h g^{-1} at 5.0 and 10.0 A g^{-1}, respectively), being one of the best among the reported molybdenum chalcogenide-based PIB anodes. We hope this work may provide a conceptual blueprint to show the positive effect of a collective strategy on designing high-performance PIB anode materials.

2. Experimental Section

2.1. Materials Preparation

1.0 g CNTs were acid-treated in a mixture of HNO_3/H_2SO_4 solution with a volume ratio of 1:3, and this mixture was refluxed with stirring vigorously for 3 h at 70 °C. Afterward, the acid-treated CNTs (HCNTs) were filtrated and rinsed with deionized (DI) water until the pH value was close to neutral and then dried in a vacuum at 60 °C overnight. The ultrathin $MoSe_2$ nanosheets coated CNTs composite was synthesized by a solvothermal method. In a typical procedure, 10.0 mg HCNTs were ultrasonically dispersed in a 25.0 mL mixture of DI water and absolute ethanol (2:3 vol%), and then 0.309 g Na_2MoO_4 was added into the mixture. Separately, 0.236 g selenium powders were dissolved in 5.0 mL $N_2H_4 \cdot H_2O$ to form a dark red solution in an air atmosphere. Thereafter, the hydrazine hydrate-Se solution was slowly dropped into the Na_2MoO_4-HCNTs solution with magnetic stirring. After 30 min, the mixture was transferred into a Teflon-lined stainless-steel autoclave and heated at 180 °C for 12 h. After cooling to room temperature, the product was rinsed with DI water and ethanol several times by centrifuging and dried in a vacuum at 60 °C overnight. To improve the crystallinity, the obtained powders were annealed in a nitrogen atmosphere at 600 °C for 3 h with a ramping rate of 5 °C min^{-1}; the final product was namely $MoSe_2$@CNTs. For comparison, pure $MoSe_2$ was prepared by the same method without adding HCNTs, and low-crystallized $MoSe_2$ (L-$MoSe_2$) was synthesized by a simplex solvothermal process without annealing.

2.2. Material Characterization

The morphology of the samples was measured by field-emission scanning electron microscopy (SEM, Zeiss AURIGA). The microstructure, element composition, and crystal lattice were characterized by FEI Titan 80-300 aberration-corrected transmission electron microscopy (TEM). The crystallographic structure was recorded on X-ray diffraction (XRD, X'Pert-Pro MPD). The information on chemical bonding was investigated by Raman spectroscopy with laser excitation at 532 nm (inVia Raman microscope). The surface chemistry information was analyzed by X-ray photoelectron spectroscopy (XPS, ESCALAB MK II). Thermogravimetric analysis (TGA) was carried out from 100 to 700 °C under a flow of air.

2.3. COMSOL Simulation

The simulation of electric field distribution in electrodes was carried out by using software of COMSOL Multiphyics (ACDC module of simple resistor). The steady-state electric property in simulation obeys the following current conservation equations:

$$\nabla \cdot J = 0 \tag{1}$$

$$J = \sigma E \tag{2}$$

$$E = -\nabla V \tag{3}$$

where J, E, and V are current density, electric field, and electric potential in the electrode, respectively. The electric conductance (σ) of the electrode materials (i.e., $MoSe_2$ and CNTs) are obtained from the software database. A three-dimensional layout was used for simulation and the geometrical parameters (e.g., the diameter of the core CNTs and the thickness of the shell $MoSe_2$) of the nanocomposite electrode are obtained from the corresponding SEM images. The electrodes are set to be squarely arranged and the periodicity (namely, inter-electrode distance) is in accordance with the experimental observation. Meanwhile, a planar $MoSe_2$ film with the same thickness as that of the nanocomposite electrode was used for comparison.

2.4. Electrochemical Measurements

The working electrode was prepared by mixing the active materials, Super P, and carboxymethyl cellulose sodium at a weight ratio of 7:2:1 in DI water. The mixture was uniformly coated on a copper foil with a mass loading of 1–2 mg cm^{-2}, and then it was dried in a vacuum oven at 105 °C for 12 h. Electrochemical measurements were conducted using CR2032 coin cells. The coin cell was assembled in a nitrogen-filled glovebox with oxygen and moisture contents less than 0.1 ppm.

Metallic potassium as a counter electrode was separated from the working electrode by a glass fiber membrane (Whatman, Grade GF/B). 3.0 M potassium bis(fluorosulfonyl)imide in dimethoxyethane was employed as an electrolyte. Galvanostatic discharge/charge measurement was performed on a Land CT 2001A battery testing system (Land, China) at different current densities in a voltage range of 0.01–3.0 V at room temperature. Cyclic voltammetry (CV) and electrochemical impedance spectroscopy (EIS) were carried out on a VSP electrochemical workstation (Bio-Logic, France).

3. Results and Discussion

The preparation procedure of $MoSe_2$@CNTs is briefly displayed in **Scheme 1**. Firstly, CNTs were acid-treated by a mixing acid solution and thus a plentiful of hydroxyl and carboxyl groups were grown on the surface of CNTs. Afterward, HCNTs mixed with the selenium and molybdenum sources were reacted under a facile solvothermal condition. Owing to the groups of HCNTs, the $MoSe_2$ nanosheet was anchored on CNTs, exhibiting an ultrathin feature. Finally, to improve the crystallinity of the $MoSe_2$ nanosheets, the obtained products from the solvothermal process were annealed in an inert atmosphere.

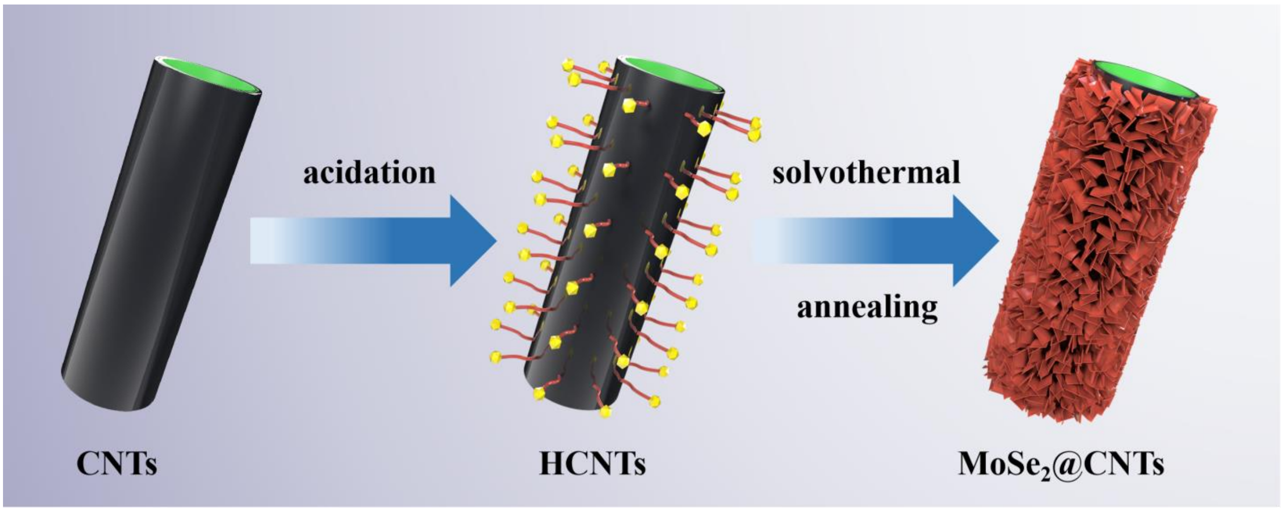

Scheme 1. Schematic illustration for the preparation of $MoSe_2$@CNTs.

The morphology characterization of the samples was implemented by SEM. CNTs have a 1D structure with a monodisperse diameter of ~20 nm and display smooth surfaces (**Figure S1**). **Figure 1a** shows the pure $MoSe_2$, it is visible that the nanosheets stack closely into a flower-like spherical architecture with several hundred nanometers in size. In regard to $MoSe_2$@CNTs, the corrugated $MoSe_2$ nanosheets have been perpendicularly coated on the surface of CNTs without obvious aggregation (**Figure 1c** and **S2**), exhibiting an ultrathin characteristic with a thickness range of 3–5 nm, which can be attributed to the fact that CNTs provide a good supporter to anchor the edge-oriented $MoSe_2$ nanosheets, thus largely restraining the $MoSe_2$ nanosheets from stacking (see the inset in **Figure 1c**).[28, 29] In such a 2D-1D heterostructure, the 2D ultrathin $MoSe_2$ nanosheets can expose abundant active edges for K^+ adsorption and largely shorten K^+ diffusion length, meanwhile, 1D CNTs can serve as good conducive pathways for electrons.[28, 30, 31]

The microstructure of the as-obtained samples was examined by high-resolution transmission electron microscopy (HRTEM). The $MoSe_2$ nanosheets in both samples display a typical lamellar structure, as depicted in **Figure 1b** and **1d**. It is noteworthy that the pure $MoSe_2$ possesses a standard value of interlayer spacing (0.65 nm), corresponding to the (0 0 2) lattice spacing, while the interlayer spacing of the ultrathin $MoSe_2$ nanosheets in $MoSe_2$@CNTs slightly increases to 0.68 nm. This phenomenon was commonly observed by the studies on 2D TMC-based composites, which could be attributed to the twisted crystal structure and nanonization of $MoSe_2$.[28, 29, 32, 33] The expanded interlayer spacing is conducive to enhancing the intrinsic diffusivity of K^+.[34] Meantime, a lattice spacing of 0.28 nm, corresponding to the (1 0 0) plane of hexagonal $MoSe_2$, is measured in both samples (the inset in **Figure 1b** and **1d**), and the lattice fringes are aligned high-orderly. In the case of L-$MoSe_2$, it has a similar flower-like layered structure to the pure $MoSe_2$ (**Figure S3**), however, its lattice fringes are disordered in the majority of microareas (**Figure S4**), confirming its low crystallinity. The elemental mapping images reveal that molybdenum and selenium elements overlap with each other and uniformly distribute on the whole surface of CNTs (**Figure 1e**).

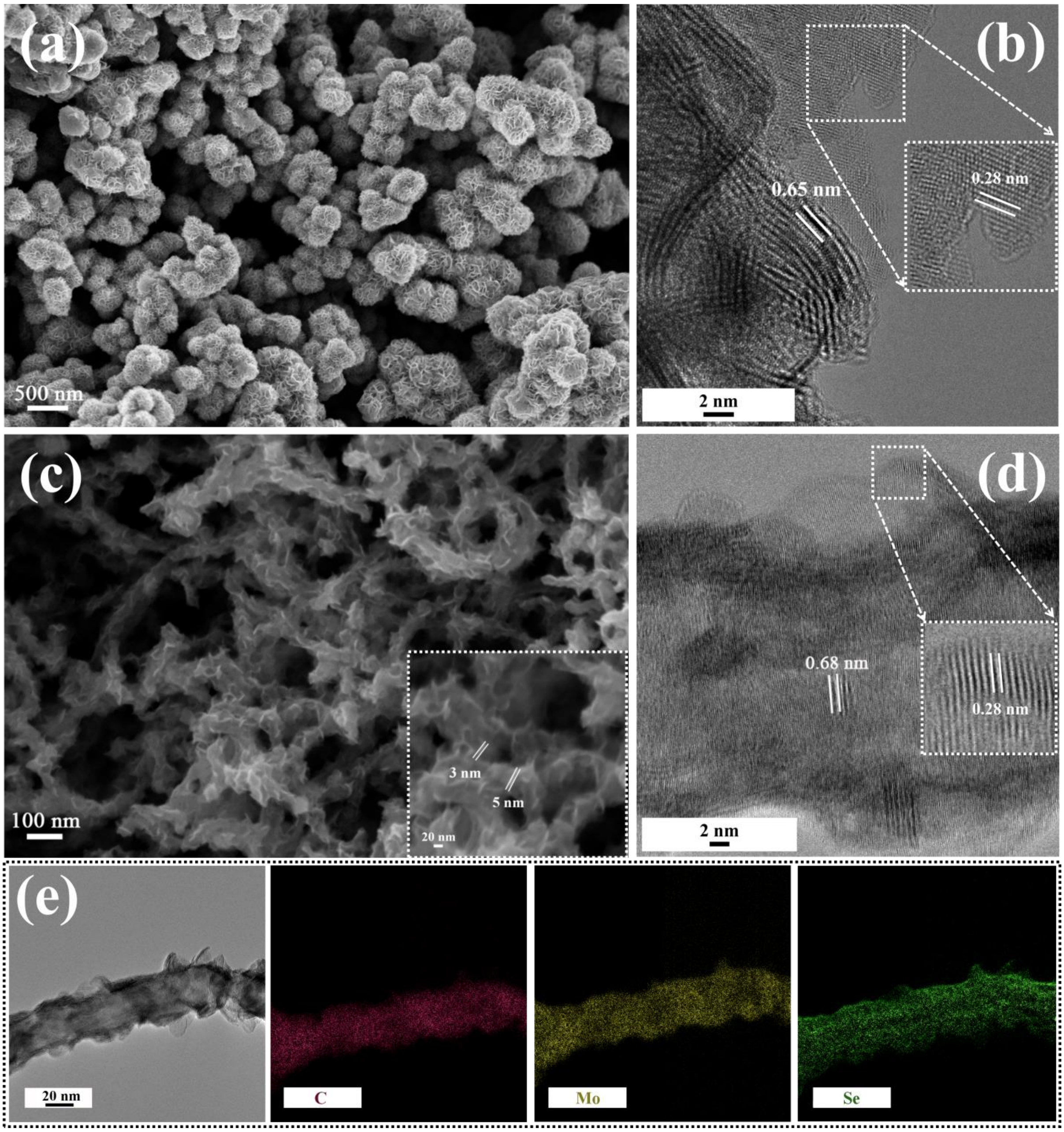

Figure 1. (a) SEM and (b) TEM images of the pure $MoSe_2$. (c) SEM and (d) TEM images of $MoSe_2$@CNTs. (e) Elemental mapping images of $MoSe_2$@CNTs.

The crystalline structure was characterized by XRD, as shown in **Figure 2a**. All the diffraction peaks of both samples are well indexed to 2H-$MoSe_2$ (JCPDS no. 29-0914), suggesting a high purity phase of $MoSe_2$. Notably, the relative intensity of (0 0 2) diffraction plane of $MoSe_2$@CNTs is weaker than that of the pure $MoSe_2$, which could be ascribed to the ordered structure and ultrathin feature of the $MoSe_2$ nanosheets.[28] Meanwhile, the crystal facial plane at (0 0 2) of $MoSe_2$@CNTs ($2\theta = 13.0°$, corresponding to 6.8 Å) has a slight shift towards the lower Bragg angle compared to that of the pure $MoSe_2$ ($2\theta = 13.5°$, corresponding to 6.5 Å), signifying the expanded interlayer spacing of the ultrathin $MoSe_2$ nanosheets in $MoSe_2$@CNTs, which is in good accordance with the HRTEM results.[35] Besides, a small broad hump at 26.3° (indicated by a purple diamond) in the pattern of $MoSe_2$@CNTs can be indexed to the (0 0 2) plane of CNTs. In stark contrast, as displayed in **Figure S5**, L-$MoSe_2$ has more broadened peaks and lower peak intensity, confirming its lower crystallinity and a high-disordered structure.

Raman spectrum was used to study structural information and characteristics (**Figure 2b**). Both samples have similar characteristic peaks that belong to the mode of $MoSe_2$ in the frequency range, however, the intrinsic absorption distinction between $MoSe_2$ and CNTs to the Raman laser leads to the result that the peak intensity of $MoSe_2$@CNTs is weaker than that of the pure $MoSe_2$.[24] The signals at 239.8 and 284.9 cm^{-1} represent the out-of-plane mode (A_{1g}) and in-plane mode (E^1_{2g}) of 2H-$MoSe_2$, respectively.[36, 37] In the high-frequency range, two distinct broad peaks located at around 1352 and 1595 cm^{-1} are observed in $MoSe_2$@CNTs but are absent for the pure $MoSe_2$. These two peaks are responsible for the D-band and G-band of CNTs, respectively.[37, 38] XPS was performed to reveal the chemical composition and bonding state. The XPS survey spectrum shows the existence of Mo, Se, and C in $MoSe_2$@CNTs (**Figure S6**). The high-resolution C 1s spectrum (**Figure 2c**) is deconvoluted into C-O (286.5 eV) C-C (284.4 eV), and C-Mo (282.5 eV).[39] In the Mo 3d spectrum (**Figure 2d**), two obvious peaks located at 231.7 and 228.6 eV are assigned to Mo $3d_{3/2}$ and Mo $3d_{5/2}$, The Se 3d spectrum in **Figure 2e** is fitted by two peaks with binding energies of 55.2 and 54.3 eV that correspond to Se $3d_{3/2}$ and Se $3d_{5/2}$.[39, 40] Both Mo 3d and Se 3d spectra of $MoSe_2$@CNTs possess similar chemical states to those of the pure $MoSe_2$ (**Figure S7**). The Raman and XPS results indirectly verify the formation of $MoSe_2$@CNTs and reveal the interface synergistic effect between the $MoSe_2$ nanosheets and CNTs.[41]

TGA was used to ascertain the component content of $MoSe_2$@CNTs. As presented in **Figure 2f**, a major weight changing takes place between 300 and 500 °C. Therein, the weight increase before

350 °C arises from the formation of SeO_2 and MoO_3 during the oxidation of $MoSe_2$. Along with the further rise of temperature, the significant weight decrease is due to the gasification of SeO_2 and the combustion of CNTs. When the temperature reaches 500 °C, the weight remains constant, which implies that the oxidation is completed. The residual weight belongs to MoO_3. According to the calculation by Equation S1, the content of $MoSe_2$ in $MoSe_2$@CNTs is 81.55%.

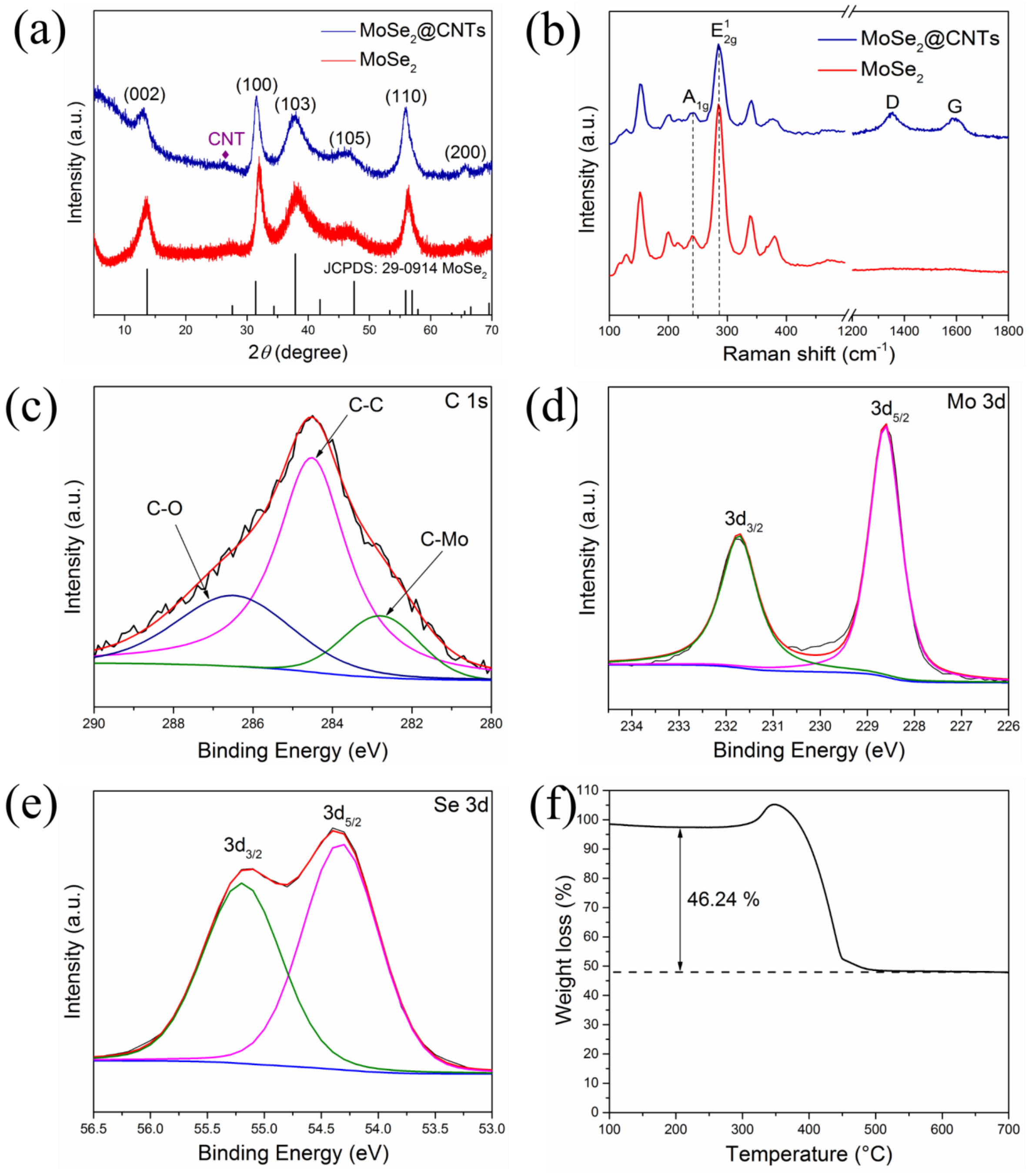

Figure 2. (a) XRD patterns and (b) Raman spectrum of $MoSe_2$@CNTs and the pure $MoSe_2$. (c) High-resolution XPS spectra of (d) C 1s, (e) Mo 3d, and (d) Se 3d of $MoSe_2$@CNTs. (f) TGA curve of $MoSe_2$@CNTs.

Galvanostatic tests were used to study K^+ storage performance with a voltage window of 0.01–3.0 V. In this range, both intercalation and conversion reactions contribute to the K^+ storage of $MoSe_2$. We first investigated the effect of crystallinity by comparing the rate capability of the pure $MoSe_2$ with that of L-$MoSe_2$. As shown in **Figure 3a**, when cycled stepwise at 0.1, 0.2, 0.5, 1.0, 2.0, and 5.0 A g^{-1}, the pure $MoSe_2$ delivers reversible capacities of 310.1, 297.2, 261.1, 217.5, 193.0 and 161.1 mAh g^{-1}. Even at a high current density of 10.0 A g^{-1}, the capacity still maintains 137.5 mAh g^{-1}. In contrast, although L-$MoSe_2$ delivers higher reversible capacities than those of the pure $MoSe_2$ at relatively low current densities (370.9, 333.8, 270.7, and 227.9 mAh g^{-1} at 0.1, 0.2, 0.5, and 1.0 A g^{-1}, respectively), only capacities of 176.0 and 80.5 mAh g^{-1} are achieved when cycled at high current densities of 2.0 and 5.0 A g^{-1} (**Figure S8**). This phenomenon matches well with the result of our previous study, that is, the high crystallinity can remain structural integrity of molybdenum dichalcogenides when intercalation and conversion reactions both contribute to the K^+ storage, thus resulting in higher capacities at high rates.[27] The $MoSe_2$@CNTs electrode was cycled at the same current densities with the pure $MoSe_2$ (**Figure 3a**). It exhibits reversible capacities of 354.8, 339.4, 293.0, 264.4, 245.3, 209.7, and 186.1 mAh g^{-1} at 0.1, 0.2, 0.5, 1.0, 2.0, 5.0, and 10.0 A g^{-1}, respectively. When the rate was reverted to 0.1 A g^{-1}, a specific capacity of 401.2 mAh g^{-1} is obtained. This rate capability is one of the best among the reported results on molybdenum dichalcogenide-based PIB anodes (**Figure 3b** and **Table S1**).[6, 40, 42-48] CNTs as a control group were cycled at the same rate range of 0.1–10.0 A g^{-1} (**Figure S9**). It is obvious that the capacities at each current density are much lower than those of $MoSe_2$@CNTs, meaning that the $MoSe_2$ nanosheets in $MoSe_2$@CNTs make the major contribution to the K^+ storage.

The electrochemical behavior of the samples is also revealed by comparing galvanostatic discharge-charge profiles, as presented in **Figure S10**. L-$MoSe_2$ exhibits three semi-plateaus (＞1.12, 1.12–0.34, and ＜0.34 V) during discharge and two slopes (1.45 and 2.0 V) during charge. As for the pure $MoSe_2$, it shows two well-defined discharge plateaus (0.88 and 0.31 V) and a slope towards 0.01 V during discharge and a plateau at 1.53 V during charge. It is clear to see that three areas present in the discharge profiles of both the pure $MoSe_2$ and L-$MoSe_2$ (marked by the red dotted lines); they correspond to the process of intercalation, conversion, and interfacial reactions, respectively.[49] The higher and wider insertion potential of L-$MoSe_2$ is attributed to its numerous disordered structures and defects providing spaces for the insertion of K^+ at relatively higher potential during the potassiation.[50] These disordered structures and defects are also responsible for the higher initial capacity.[51] Meanwhile, the $MoSe_2$@CNTs sample with high crystallinity exhibits a similar discharge-charge profile with the pure $MoSe_2$. Additionally, the electrochemical property of $MoSe_2$@CNTs was investigated by CV measurement. The initial three CV curves of $MoSe_2$@CNTs with a scan rate of 0.1 mV s^{-1} are depicted in **Figure 3c**. In the first cathodic sweep, two reduction peaks at 0.81 and 0.24 V are observed. The peak of 0.81 V could be correlated to the intercalation of K^+ into the interlayer of $MoSe_2$, resulting in the formation of K_xMoSe_2. And the peak of 0.24 V could be associated with the conversion reaction of K_xMoSe_2 to Mo metal and K-Se compound, as well as the formation of irreversible solid electrolyte interphase (SEI) layers. In the subsequent anodic sweep, an oxidation peak appearing at 1.77 V could be related to the extraction of K^+. From the second cycle onward, the initial two reduction peaks vanish and a new peak emerges at 1.13 V, meanwhile, the anodic peak shifts to 1.80 V, which could account for the structure changing of $MoSe_2$.[40, 52, 53] After the first discharge-charge process, the CV curves overlap very well, implying the high reversibility of $MoSe_2$@CNTs after the initial potassiation-depotassiation. The small difference in voltage position between the galvanostatic discharge-charge profiles and the CV curves could be ascribed to the different measurement systems, in which the slow scan rate in the

CV testing can provide enough time to complete the oxidation-reduction process, whereas the higher current density used in the galvanostatic measurement leads to the inadequate electrochemical redox reaction.[54]

Cycling stability as an important parameter for rechargeable ion batteries was investigated in our case. $MoSe_2$@CNTs and the pure $MoSe_2$ were cycled at a current density of 0.1 A g^{-1}. After the first cycle, the discharge plateaus at 0.88 and 0.31 V are replaced by a plateau at about 1.25 V (**Figure S11**), while the charge plateaus are retained. These plateaus can be kept till 100 cycles in $MoSe_2$@CNTs, whereas the plateaus are gradually unobvious in the pure $MoSe_2$. In the initial cycle, the discharge/charge capacities of $MoSe_2$@CNTs are 543.8/376.9 mAh g^{-1}, corresponding to Coulombic efficiency (CE) of 69.30%. In the second cycle, the discharge and charge capacities decreased to 371.5 and 347.7 mAh g^{-1}, respectively, while the CE increases to 93.53%. The low initial CE and capacity loss are most likely caused by the decomposition of the electrolyte and the formation of SEI layers.[6, 40] After 100 cycles, as shown in **Figure 3d**, the $MoSe_2$@CNTs electrode remains a capacity of 320.9 mAh g^{-1} with a capacity retention of 86.4%, which still reaches 76% of the theoretical capacity of $MoSe_2$ (422.3 mAh g^{-1}, as shown in Equation S2). As for the pure $MoSe_2$ electrode, it displays a relatively low initial discharge capacity of 485.4 mAh g^{-1}, and the capacity falls to 325.1 mAh g^{-1} in the second cycle. Besides, it only maintains a capacity of 121.8 mAh g^{-1} at the 100th cycle, corresponding to 37.5% retention. Additionally, the stability of $MoSe_2$@CNTs at a high current density was studied by cycling at 2.0 A g^{-1} after 10 cycles at 0.1 A g^{-1} (**Figure 3e**). It retains 203 mAh g^{-1} and 159 mAh g^{-1} after 100 and 200 cycles, respectively, with the CE of > 99%.

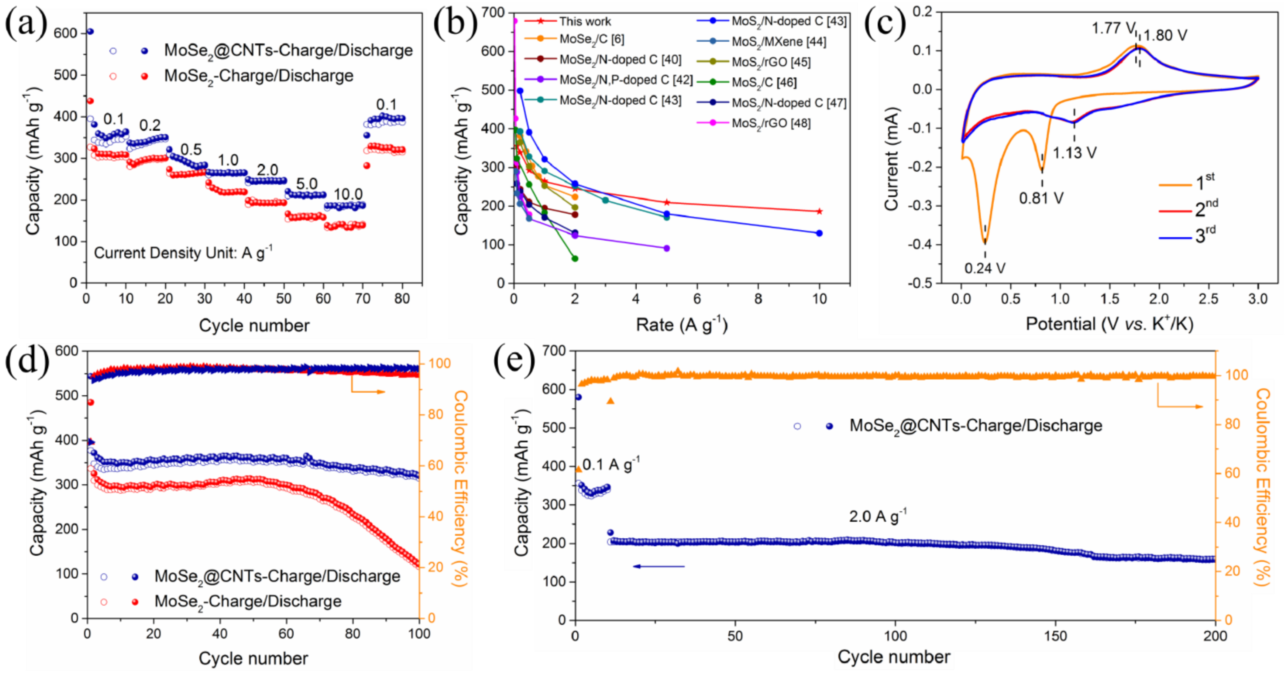

Figure 3. (a) Rate capability of MoSe$_2$@CNTs and the pure MoSe$_2$. (b) Comparison of the rate capability of MoSe$_2$@CNTs and previously reported molybdenum chalcogenides. (c) CV curves of MoSe$_2$@CNTs at 0.1 mV s^{-1}. (d) Cycling performance of MoSe$_2$@CNTs and the pure MoSe$_2$ at 0.1 A g^{-1}. (e) Cycling performance of MoSe$_2$@CNTs at 2.0 A g^{-1}.

In comparison to the pure MoSe$_2$, MoSe$_2$@CNTs exhibit better electrochemical performance, especially rate capability. Except for the structural features that were shown in **Figure 1**, the superior conductivity provided by CNTs serves as a critical role. To illustrate the effect of CNTs, a simulation of electric field distribution was conducted by COMSOL. The model set-up such as geometrical features of CNTs and MoSe$_2$ was obtained from the SEM and TEM images. **Figure 4a** and **4b** show the cross-sectional electric field maps of MoSe$_2$ without and with CNTs modification, respectively. Obviously, the electric field of the MoSe$_2$ coated at CNTs is about 3.5–6.0 times higher than that of the pure MoSe$_2$ counterpart. The enhanced electric field is of great significance for electron transportation, leading to the improvement of the electrochemical performance. EIS was further carried out to elucidate the effect of CNTs. **Figure S12** shows the Nyquist plots of MoSe$_2$@CNTs and the pure MoSe$_2$ recorded after 10 and 50 cycles. They consist of a semicircle at high-to-medium frequency ranges and a tail at low frequency regions, which refer to charge transfer resistance (R_{ct}) and K ion diffusion.[55, 56] The impedance data could be fitted by an equivalent circuit shown in the insert of **Figure S12**. It is evident that the $MoSe_2$@CNTs electrode exhibits smaller R_{ct} values as compared to the pure $MoSe_2$ regardless of cycles. The R_{ct} values of the $MoSe_2$@CNTs electrode after 10 and 50 cycles are 2797 and 3223 Ω, respectively, whereas the resistances of the pure $MoSe_2$ reach 4061 Ω at the 10th cycle and 4749 Ω at the 50th cycle, which indicate the enhanced conductivity and reduced charge transfer resistance of the $MoSe_2$@CNTs electrode.[57, 58] We noticed that a recent work reported $MoSe_2$ nanosheets anchored N-doped carbon nanotubes, where polypyrrole was employed as a carbon precursor.[59] However, the delivered electrochemical performance is lower than that of this work to a large degree. Herein, two advantages derived from CNTs could elucidate the reason: (1) in comparision to other carbonaceous materials (e.g. graphite and carbon black), CNTs as a conductive additive for anode materials provide a more effective scheme to introduce electron transmission pathways in electrodes with a relatively low content, therefore, the ratio of main active material in CNT-based composites is much higher, which is beneficial to increase the energy density of the cell;[60] (2) the comparison of the electrical conductivity of CNTs with that of the vast majority of carbon materials shows that CNTs are at an advantage, while the remarkable electrical conductivity of electrodes is one of prerequisites for ion batteries with high-rate performance.[61]

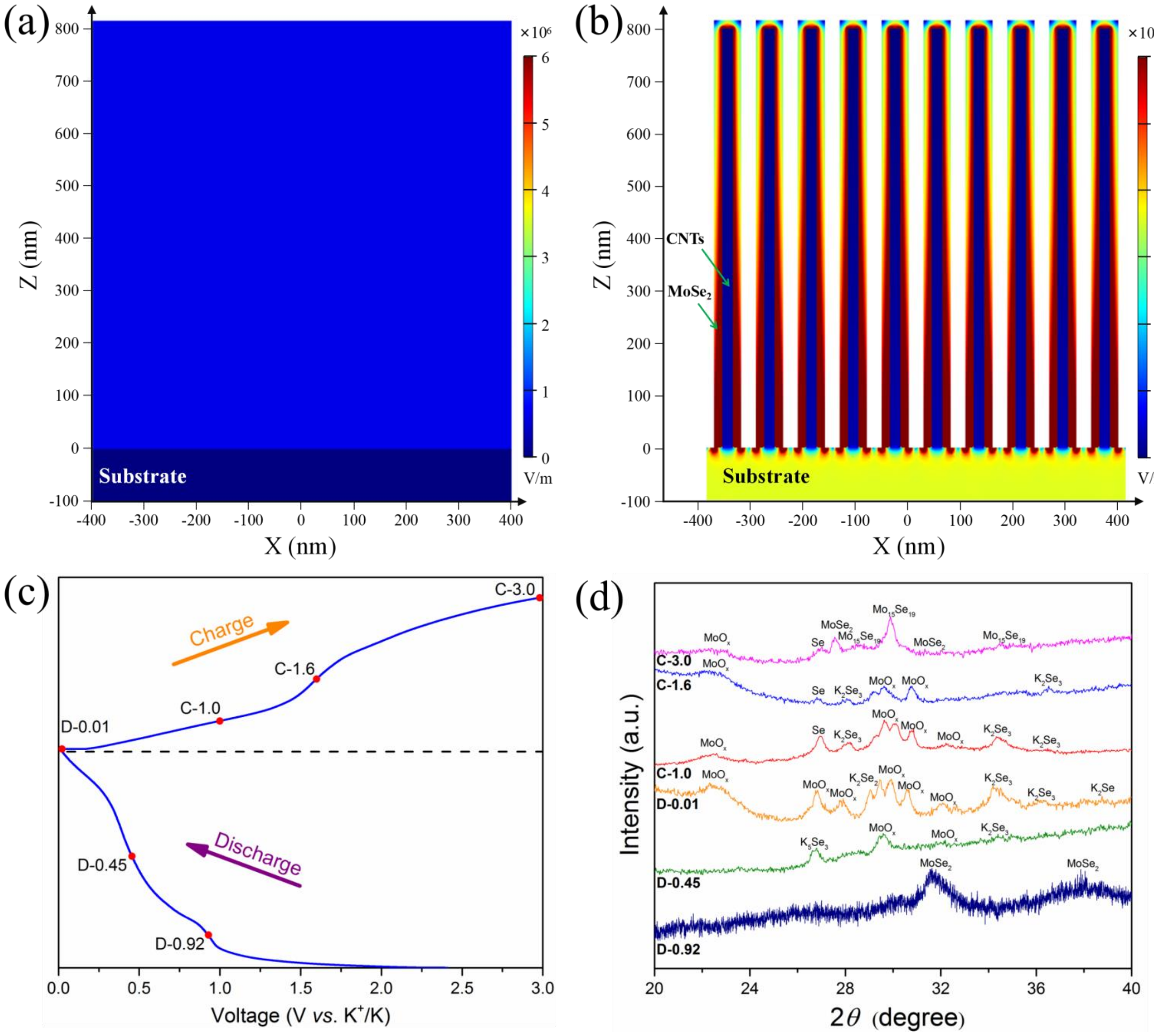

Figure 4. COMSOL simulated electric field distributions of (a) the pure $MoSe_2$ and (b) $MoSe_2$@CNTs. (c) Discharge-charge profiles of $MoSe_2$@CNTs of the first cycle and (d) XRD patterns of $MoSe_2$@CNTs electrodes at different discharge-charge states.

The K^+ storage mechanism of $MoSe_2$@CNTs was verified by ex situ XRD. Six same cells were stopped at different states during the first discharge/charge process (**Figure 4c**), and then disassembled in the glove box. Subsequently, the electrodes were dried in the vacuum chamber and measured by XRD (**Figure 4d**). When discharging to 0.92 V, the characteristic peaks of $MoSe_2$ still exist and no new peaks are detected, implying that only an intercalation-type electrochemical reaction occurs. As further discharging to 0.45 V, all the peaks attributed to $MoSe_2$ vanish, and the peaks of molybdenum oxide and K-Se compounds (K_5Se_3 and K_2Se_3) appear, among which the molybdenum oxide may result from the oxidation of Mo during the ex situ XRD testing in an air atmosphere.[15, 62] At the end of discharge, a weak peak at 38.7° indexed to K_2Se was detected. In the charging process, the peaks of the molybdenum oxide and K-Se compounds weaken gradually, at the same time, some new peaks assigned to Se and $Mo_{15}Se_{19}$ are found. When the electrode was fully charged to 3.0 V, the peaks of $MoSe_2$ reappeared, but the peak at 22.5° of the molybdenum oxide not fully disappeared. These results well match the CV curves and indicate that the K^+ storage mechanism of $MoSe_2$ is a partially reversible conversion reaction.

The kinetics of $MoSe_2$@CNTs was analyzed based on the CV measurement at scan rates ranging from 0.1 to 1.0 mV s^{-1}. As the scan rate increases, the CV curves keep the same outlines, and the depotassiation peaks broaden and cover higher potential ranges, implying the existence of capacitive behavior (**Figure 5a**).[63, 64] The following Equation 4 can be used to verify this speculation, where the peak current (i) obeys a power-law relationship with the scan rate (v).

$$i = av^b \tag{4}$$

$$log(i) = blog(v) + log(a) \tag{5}$$

where a and b values are adjustable parameters. The b value could be determined by the slope of log(i) versus log(v) (Equation 5) and provide information about charge storage behavior. Generally, electrochemical processes are dominated by diffusion-controlled behavior when b value closes to 0.5, while b value is about 1.0 suggesting a capacitive process.[63, 65] In our case, the b values of the anodic and cathodic peaks are 0.88 and 0.86, respectively, signifying the synergistic contribution of diffusion-controlled and capacitive processes (**Figure 5b**).[21, 66] The following Equations 6–7 are used to quantitatively analyze the contribution from the mixed behaviors.

$$i = k_1v + k_2v^{1/2} \tag{6}$$

$$i/v^{1/2} = k_1v^{1/2} + k_2 \tag{7}$$

where k_1 and k_2 can be determined by plotting $v^{1/2}$ versus $i/v^{1/2}$. $k_1v^{1/2}$ represents the quantity of diffusion-controlled process, and k_2v denotes the contribution of capacitive behavior. **Figure 5c** shows the calculated capacitive contribution ratio of 85.8% at a scan rate of 1.0 mV s^{-1}. A summary of contribution at different scan rates is plotted in **Figure 5d**. The percentage of capacitive contributions are 65.2%, 69.7%, 75.3%, 78.8%, 82.1%, and 85.8%, respectively, when the scan rate increases from 0.1 to 1.0 mV s^{-1}. As is well-known, the higher capacitive contribution is favorable for fast ion storage kinetics, thus electrode materials can exhibit better rate performance. However, the majority of previous works on metal chalcogenide-based PIB anodes possess limited capacitance contributions (＜ 80%), even at very high rates.[21, 66-69] Generally, to achieve high capacitive contribution, the electrode material should meet three prerequisites: (1) fast mass transport originated from short ion diffusion pathways and low ion diffusion resistances; (2) rapid electron transfer within entire electrodes; (3) easily available active surface areas.[30, 31] Our heterostructured $MoSe_2$@CNTs are in line with these three requirements, as illustrated in **Figure S13**, thus delivering a high capacitance capacity contribution even at a low scan rate of 0.8 mV s^{-1}.

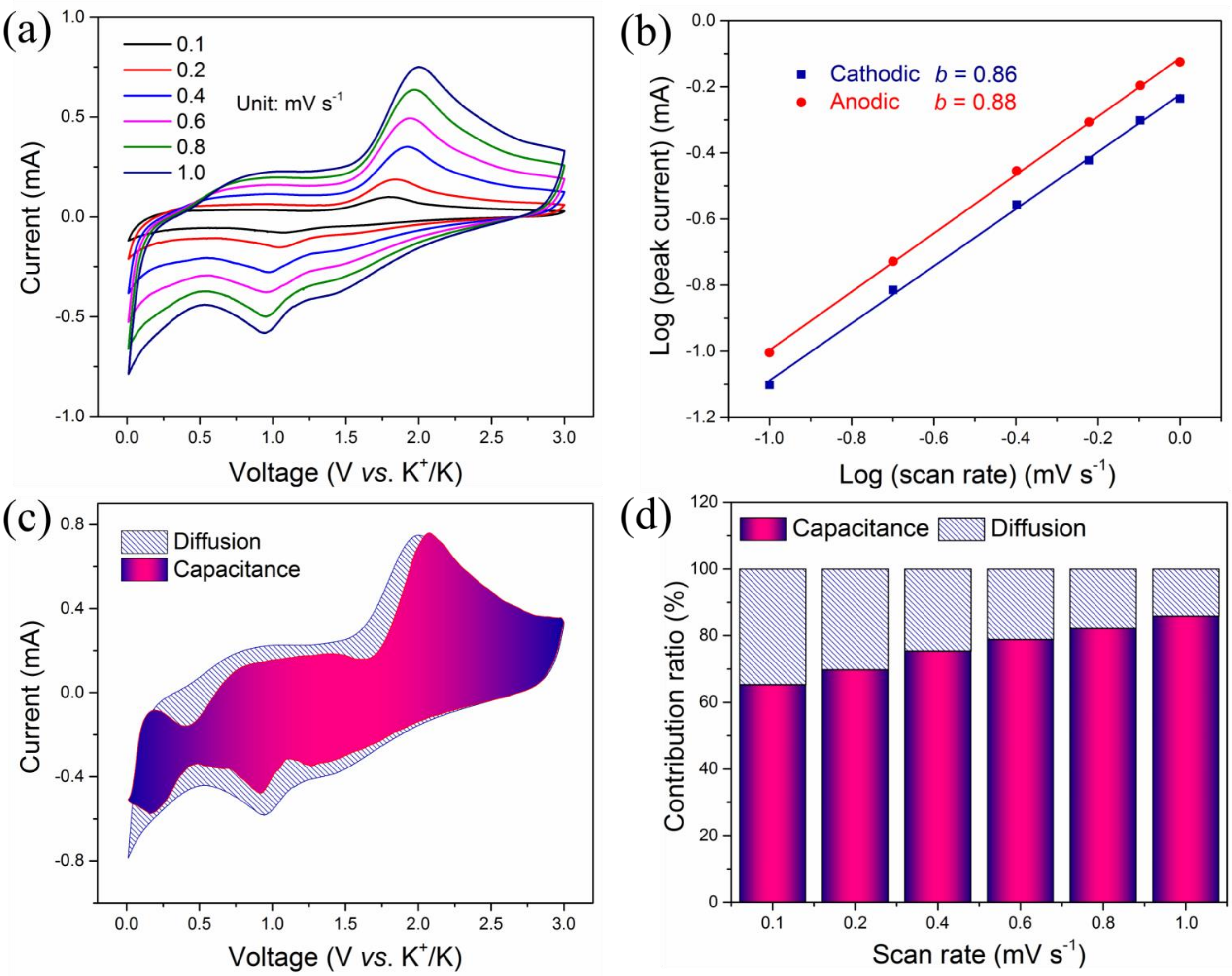

Figure 5. (a) CV profiles of $MoSe_2$@CNTs at different scan rates. (b) Functional relationship of the peak current (*i*) *vs.* the scan rate (*v*). (c) Sketch view of the capacitive contribution ratio at a scan rate of 1.0 mV s^{-1}. (d) Capacitive contribution ratios at different scan rates.

4. Conclusion

In summary, we synthesized a heterostructure of 2D high-crystallized ultrathin $MoSe_2$ nanosheets coated 1D multiwall carbon nanotubes and employed it as an anode material for PIBs to reveal the positive effect of a collective strategy for optimizing the K storage capability of 2D TMCs. In this nanocomposite, CNTs restrain the aggregation of $MoSe_2$ nanosheets and act as a superior conductive pathway for the electron transport, and meanwhile the ultrathin $MoSe_2$ nanosheets not only expose abundant active sites for the electrochemical reaction but also shorten the diffusion length for electrons/K ions. Furthermore, the high crystallinity of the $MoSe_2$ nanosheets, obtained by the thermal treatment which is independent and compatible with the material synthesis method, plays a positive role in enhancing the rate performance. By virtue of the combination of all these advantages, the $MoSe_2$@CNTs electrode delivered competitive rate capacities of 209.7 and 186.1 mA h g^{-1} even at high current densities of 5.0 A g^{-1} and 10.0 A g^{-1}, respectively. We hope this study could shed light on the importance of collective strategies in optimizing the electrochemical K storage capability of 2D TMCs, and meanwhile provide a novel insight into designing pluralistic electrode materials with synergistically enhanced electrochemical performance.

Associated Content

The Supporting Information is available free of charge on the ACS Publications website.

Additional material characterization of the samples in this work; discharge-charge profiles of the samples; Rate performance comparison; EIS spectra of $MoSe_2$@CNTs and pure $MoSe_2$ after different cycles; the comparison of transportation pathways for K ions and electrons.

Author Information

Corresponding Authors

*E-mail: shunwang@wzu.edu.cn (S. W.)

*E-mail: yong.lei@tu-ilmenau.de (Y. L.)

ORCID

Yuhan Wu: 0000-0002-6288-2112

Shun Wang: 0000-0001-5305-5134

Yong Lei: 0000-0001-5048-7433

Notes

The authors declare no competing financial interest.

Acknowledgements

This work is financially supported by the German Research Foundation (DFG: LE 2249/5-1) and the Sino-German Center for Research Promotion (GZ1579). Yuhan Wu would like to acknowledge the China Scholarship Council (No. 201609505011) for the financial support. This work contributes to the research performed at CELEST (Center for Electrochemical Energy Storage Ulm-Karlsruhe) and was funded by the German Research Foundation (DFG) under Project ID 390874152 (POLiS Cluster of Excellence). We would like to thank Dr. Henry Romanus and Dr. Arne Albrecht for technical support on XRD.

References

(1) Kubota, K.; Dahbi, M.; Hosaka, T.; Kumakura, S.; Komaba, S., Towards K-Ion and Na-Ion Batteries as "Beyond Li-Ion". *Chem. Rec.* **2018**, *18* (4), 459-479.

(2) Xu, Y.; Bahmani, F.; Zhou, M.; Li, Y.; Zhang, C.; Liang, F.; Kazemi, S. H.; Kaiser, U.; Meng, G.; Lei, Y., Enhancing Potassium-Ion Battery Performance by Defect and Interlayer Engineering. *Nanoscale Horiz.* **2019**, *4* (1), 202-207.

(3) Xu, R.; Du, L.; Adekoya, D.; Zhang, G.; Zhang, S.; Sun, S.; Lei, Y., Well-Defined Nanostructures for Electrochemical Energy Conversion and Storage. *Adv. Energy Mater.* **2020**, 2001537.

(4) Zhang, C.; Zhao, H.; Lei, Y., Recent Research Progress of Anode Materials for Potassium-Ion Batteries. *Energ. Environ. Mater.* **2020**, *3* (2), 105-120.

(5) Ren, X.; Zhao, Q.; McCulloch, W. D.; Wu, Y., MoS_2 as a Long-Life Host Material for Potassium Ion Intercalation. *Nano Res.* **2017**, *10* (4), 1313-1321.

(6) Wang, W.; Jiang, B.; Qian, C.; Lv, F.; Feng, J.; Zhou, J.; Wang, K.; Yang, C.; Yang, Y.; Guo, S., Pistachio-Shuck-Like $MoSe_2$/C Core/Shell Nanostructures for High-Performance Potassium-Ion Storage. *Adv. Mater.* **2018**, *30* (30), 1801812.

(7) Wu, Y.; Xu, Y.; Li, Y.; Lyu, P.; Wen, J.; Zhang, C.; Zhou, M.; Fang, Y.; Zhao, H.; Kaiser, U.; Lei, Y., Unexpected Intercalation-Dominated Potassium Storage in WS$_2$ as a Potassium-Ion Battery Anode. *Nano Res.* **2019**, *12* (12), 2997-3002.

(8) Ding, H.; Zhou, J.; Rao, A. M.; Lu, B., Cell-Like-Carbon-Micro-Spheres for Robust Potassium Anode. *Natl. Sci. Rev.* **2020**, nwaa276.

(9) Jian, Z.; Xing, Z.; Bommier, C.; Li, Z.; Ji, X., Hard Carbon Microspheres: Potassium-Ion Anode Versus Sodium-Ion Anode. *Adv. Energy Mater.* **2016**, *6* (3), 1501874.

(10) Wang, L.; Li, S.; Li, J.; Yan, S.; Zhang, X.; Wei, D.; Xing, Z.; Zhuang, Q.; Ju, Z., Nitrogen/Sulphur Co-Doped Porous Carbon Derived from Wasted Wet Wipes as Promising Anode Material for High Performance Capacitive Potassium-Ion Storage. *Mater. Today Energy* **2019**, *13*, 195-204.

(11) Zheng, N.; Jiang, G.; Chen, X.; Mao, J.; Zhou, Y.; Li, Y., Rational Design of a Tubular, Interlayer Expanded MoS$_2$–N/O Doped Carbon Composite for Excellent Potassium-Ion Storage. *J. Mater. Chem. A* **2019**, *7* (15), 9305-9315.

(12) Zhang, Q.; Mao, J.; Pang, W. K.; Zheng, T.; Sencadas, V.; Chen, Y.; Liu, Y.; Guo, Z., Boosting the Potassium Storage Performance of Alloy-Based Anode Materials via Electrolyte Salt Chemistry. *Adv. Energy Mater.* **2018**, *8* (15), 1703288.

(13) Liu, S.; Mao, J.; Zhang, Q.; Wang, Z.; Pang, W. K.; Zhang, L.; Du, A.; Sencadas, V.; Zhang, W.; Guo, Z., An Intrinsically Non-flammable Electrolyte for High-Performance Potassium Batteries. *Angew. Chem. Int. Ed.* **2020**, *59* (9), 3638-3644.

(14) Zhang, Q.; Wang, Z.; Zhang S.; Zhou, T.; Mao, J.;·Guo, Z., Cathode Materials for Potassium‑Ion Batteries: Current Status and Perspective. *Electrochem. Energy Rev.* **2018**, *1* (4): 625-658.

(15) Jia, G.; Wang, H.; Chao, D.; He, H.; Tiep, N. H.; Zhang, Y.; Zhang, Z.; Fan, H. J., Ultrathin $MoSe_2$@N-Doped Carbon Composite Nanospheres for Stable Na-Ion Storage. *Nanotechnology* **2017**, *28* (42), 42LT01.

(16). He, H.; Huang, D.; Gan, Q.; Hao, J.; Liu, S.; Wu, Z.; Pang, W. K.; Johannessen, B.; Tang, Y.; Luo, J. L.; Wang, H.; Guo, Z., Anion Vacancies Regulating Endows MoSSe with Fast and Stable Potassium Ion Storage. *ACS Nano* **2019**, *13* (10), 11843-11852.

(17) Gu, C.; Guan, W.; Cui, Y.; Chen, Y.; Gao, L.; Huang, J., Preparation of Three-Dimensional Nanosheet-Based Molybdenum Disulfide Nanotubes as Anode Materials for Lithium Storage. *J. Mater. Chem. A* **2016**, *4* (43), 17000-17008.

(18) Zuo, X.; Chang, K.; Zhao, J.; Xie, Z.; Tang, H.; Li, B.; Chang, Z., Bubble-Template-Assisted Synthesis of Hollow Fullerene-Like MoS_2 Nanocages as a Lithium Ion Battery Anode Material. *J. Mater. Chem. A* **2016**, *4* (1), 51-58.

(19) Hu, S.; Jiang, Q.; Ding, S.; Liu, Y.; Wu, Z.; Huang, Z.; Zhou, T.; Guo, Z.; Hu, J., Construction of Hierarchical $MoSe_2$ Hollow Structures and Its Effect on Electrochemical Energy Storage and Conversion. *ACS Appl. Mater. Interfaces* **2018**, *10* (30), 25483-25492.

(20) Zheng, F.; Zhong, W.; Deng, Q.; Pan, Q.; Ou, X.; Liu, Y.; Xiong, X.; Yang, C.; Chen, Y.; Liu, M., Three-dimensional (3D) Flower-like $MoSe_2$/N-Doped Carbon Composite as a Long-Life and High-Rate Anode Material for Sodium-Ion Batteries. *Chem. Eng. J.* **2019**, *357*, 226-236.

(21) Huang, H.; Cui, J.; Liu, G.; Bi, R.; Zhang, L., Carbon-Coated $MoSe_2$/MXene Hybrid Nanosheets for Superior Potassium Storage. *ACS Nano* **2019**, *13* (3), 3448-3456.

(22) Jeong, S. Y.; Park, S.-K.; Kang, Y. C.; Cho, J. S., One-Dimensional Nanostructure Comprising $MoSe_2$ Nanosheets and Carbon with Uniformly Defined Nanovoids as an Anode for High-Performance Sodium-Ion Batteries. *Chem. Eng. J.* **2018**, *351*, 559-568.

(23) Zhang, Q.; Cheng, X.; Wang, C.; Rao, A. M.; Lu, B., Sulfur-Assisted Large-Scale Synthesis of Graphene Microspheres for Superior Potassium-Ion Batteries. *Energy Environ. Sci.* **2021**, *14* (2), 965-974.

(24) Tang, Y.; Zhao, Z.; Wang, Y.; Dong, Y.; Liu, Y.; Wang, X.; Qiu, J., Carbon-Stabilized Interlayer-Expanded Few-Layer $MoSe_2$ Nanosheets for Sodium Ion Batteries with Enhanced Rate Capability and Cycling Performance. *ACS Appl. Mater. Interface*s **2016**, *8* (47), 32324-32332.

(25) Yi, X.; Ge, J.; Zhou, J.; Zhou, J.; Lu, B., $SbVO_4$ Based High Capacity Potassium Anode: a Combination of Conversion and Alloying Reactions. *Sci. China Chem.* **2020**, *64* (2), 238-244.

(26) Ren, W.; Zhang, H.; Guan, C.; Cheng, C., Ultrathin MoS_2 Nanosheets@Metal Organic Framework-Derived N-Doped Carbon Nanowall Arrays as Sodium Ion Battery Anode with Superior Cycling Life and Rate Capability. *Adv. Funct. Mater.* **2017**, *27* (32), 1702116.

(27) Dong, Y.; Xu, Y.; Li, W.; Fu, Q.; Wu, M.; Manske, E.; Kroger, J.; Lei, Y., Insights into the Crystallinity of Layer-Structured Transition Metal Dichalcogenides on Potassium Ion Battery Performance: A Case Study of Molybdenum Disulfide. *Small* **2019**, *15* (15), 1900497.

(28) Pang, Y.; Zhang, S.; Liu, L.; Liang, J.; Sun, Z.; Wang, Y.; Xiao, C.; Ding, D.; Ding, S., Few-layer MoS_2 Anchored at Nitrogen-Doped Carbon Ribbons for Sodium-Ion Battery Anodes with High Rrate Performance. *J. Mater. Chem. A* **2017**, *5* (34), 17963-17972.

(29) Lim, Y. V.; Wang, Y.; Kong, D.; Guo, L.; Wong, J. I.; Ang, L. K.; Yang, H. Y., Cubic-Shaped WS_2 Nanopetals on a Prussian Blue Derived Nitrogen-Doped Carbon Nanoporous Framework for High Performance Sodium-Ion Batteries. *J. Mater. Chem. A* **2017**, *5* (21), 10406-10415.

(30) Zhao, C.; Yu, C.; Zhang, M.; Sun, Q.; Li, S.; Norouzi Banis, M.; Han, X.; Dong, Q.; Yang, J.; Wang, G.; Sun, X.; Qiu, J., Enhanced Sodium Storage Capability Enabled by Super Wide-Interlayer-Spacing MoS_2 Integrated on Carbon Fibers. *Nano Energy* **2017**, *41*, 66-74.

(31) Wu, J.; Lu, Z.; Li, K.; Cui, J.; Yao, S.; Ihsan-ul Haq, M.; Li, B.; Yang, Q.-H.; Kang, F.; Ciucci, F.; Kim, J.-K., Hierarchical MoS_2/Carbon Microspheres as Long-Life and High-Rate Anodes for Sodium-Ion Batteries. *J. Mater. Chem. A* **2018**, *6* (14), 5668-5677.

(32) Liu, S.; Liu, Y.; Lei, W.; Zhou, X.; Xu, K.; Qiao, Q.; Zhang, W.-H., Few-Layered ReS_2 Nanosheets Vertically Aligned on Reduced Graphene Oxide for Superior Lithium and Sodium Storage. *J. Mater. Chem. A* **2018**, *6* (41), 20267-20276.

(33) Shi, Y.; Wan, Y.; Liu, R.; Tu, B.; Zhao, D., Synthesis of Highly Ordered Mesoporous Crystalline WS_2 and MoS_2 *via* a High-Temperature Reductive Sulfuration Route. *J. Am. Chem. Soc.* **2007**, *129* (30), 9522-9531.

(34) Liu, S.; Lei, W.; Liu, Y., Rational Design of Few-Layered ReS_2 Nanosheets/N-Doped Mesoporous Carbon Nanocomposites for High-Performance Pseudocapacitive Lithium Storage. *Chem. Eng. J.* **2019**, *356*, 1052-1061.

(35) Zhang, S.; Yu, X.; Yu, H.; Chen, Y.; Gao, P.; Li, C.; Zhu, C., Growth of Ultrathin MoS_2 Nanosheets with Expanded Spacing of (002) Plane on Carbon Nanotubes for High-Performance Sodium-Ion Battery Anodes. *ACS Appl. Mater. Interfaces* **2014**, *6* (24), 21880-21885.

(36) Larentis, S.; Fallahazad, B.; Tutuc, E., Field-effect Transistors and Intrinsic Mobility in Ultra-Thin $MoSe_2$ Layers. *Appl. Phys. Lett.* **2012**, *101* (22), 223104.

(37) Luo, Z.; Zhou, J.; Wang, L.; Fang, G.; Pan, A.; Liang, S., Two-Dimensional Hybrid Nanosheets of Few Layered $MoSe_2$ on Reduced Graphene Oxide as Anodes for Long-Cycle-Life Lithium-Ion Batteries. *J. Mater. Chem. A* **2016**, *4* (40), 15302-15308.

(38) Niu, F.; Yang, J.; Wang, N.; Zhang, D.; Fan, W.; Yang, J.; Qian, Y., $MoSe_2$-Covered N,P-Doped Carbon Nanosheets as a Long-Life and High-Rate Anode Material for Sodium-Ion Batteries. *Adv. Funct. Mater.* **2017**, *27* (23), 1700522.

(39) Liu, Y.; Zhu, M.; Chen, D., Sheet-Like $MoSe_2$/C Composites with Enhanced Li-Ion Storage Properties. *J. Mater. Chem. A* **2015**, *3* (22), 11857-11862.

(40) Ge, J.; Fan, L.; Wang, J.; Zhang, Q.; Liu, Z.; Zhang, E.; Liu, Q.; Yu, X.; Lu, B., $MoSe_2$/N-Doped Carbon as Anodes for Potassium-Ion Batteries. *Adv. Energy Mater.* **2018**, *8* (29), 1801477.

(41) Chen, B.; Lu, H.; Zhao, N.; Shi, C.; Liu, E.; He, C.; Ma, L., Facile Synthesis and Electrochemical Properties of Continuous Porous Spheres Assembled from Defect-Rich, Interlayer-Expanded, and Few-Layered MoS_2/C Nanosheets for Reversible Lithium Storage. *J. Power Sources* **2018**, *387*, 16-23.

(42) Zeng, L.; Kang, B.; Luo, F.; Fang, Y.; Zheng, C.; Liu, J.; Liu, R.; Li, X.; Chen, Q.; Wei, M.; Qian, Q., Facile Synthesis of Ultra-Small Few-Layer Nanostructured $MoSe_2$ Embedded on N, P Co-Doped Bio-Carbon for High-Performance Half/Full Sodium-Ion and Potassium-Ion Batteries. *Chem. Eur. J.* **2019**, *25* (58), 13411-13421.

(43) Ma, M.; Zhang, S.; Yao, Y.; Wang, H.; Huang, H.; Xu, R.; Wang, J.; Zhou, X.; Yang, W.; Peng, Z.; Wu, X.; Hou, Y.; Yu, Y., Heterostructures of 2D Molybdenum Dichalcogenide on 2D Nitrogen-Doped Carbon: Superior Potassium-Ion Storage and Insight into Potassium Storage Mechanism. *Adv. Mater.* **2020**, *32* (22), 2000958.

(44) Li, J.; Rui, B.; Wei, W.; Nie, P.; Chang, L.; Le, Z.; Liu, M.; Wang, H.; Wang, L.; Zhang, X., Nanosheets Assembled Layered MoS_2/MXene as High Performance Anode Materials for Potassium Ion Batteries. *J. Power Sources* **2020**, *449*, 227481.

(45) Xie, K.; Yuan, K.; Li, X.; Lu, W.; Shen, C.; Liang, C.; Vajtai, R.; Ajayan, P.; Wei, B., Superior Potassium Ion Storage via Vertical MoS_2 "Nano-Rose" with Expanded Interlayers on Graphene. *Small* **2017**, *13* (42), 1701471.

(46) Jia, B.; Zhao, Y.; Qin, M.; Wang, W.; Liu, Z.; Lao, C.-Y.; Yu, Q.; Liu, Y.; Wu, H.; Zhang, Z.; Qu, X., Multirole Organic-Induced Scalable Synthesis of a Mesoporous MoS_2-Monolayer/Carbon Composite for High-Performance Lithium and Potassium Storage. *J. Mater. Chem. A* **2018**, *6* (24), 11147-11153.

(47) Jia, B.; Yu, Q.; Zhao, Y.; Qin, M.; Wang, W.; Liu, Z.; Lao, C.-Y.; Liu, Y.; Wu, H.; Zhang, Z.; Qu, X., Bamboo-Like Hollow Tubes with MoS_2/N-Doped-C Interfaces Boost Potassium-Ion Storage. *Adv. Funct. Mater.* **2018**, *28* (40), 1803409.

(48) Chong, S.; Sun L.; Shu C.; Guo, S.; Liu, Y.; Wang W.; Liu, H. K., Chemical Bonding Boosts Nano-Rose-Like MoS_2 Anchored on Reduced Graphene Oxide for Superior Potassium-Ion Storage. *Nano Energy*, **2019**, *63*, 103868.

(49) Luo, X.; Huang, J.; Li, J.; Cao, L.; Wang, Y.; Xu, Z.; Guo, L.; Cheng, Y.; Kajiyoshi, K.; Chen, S., Controlled WS_2 Crystallinity Effectively Dominating Sodium Storage Performance. *J. Energy Chem.* **2020**, *51*, 143-153.

(50) Fang, H. T.; Liu, M.; Wang, D. W.; Sun, T.; Guan, D. S.; Li, F.; Zhou, J.; Sham, T. K.; Cheng, H. M., Comparison of the Rate Capability of Nanostructured Amorphous and Anatase TiO_2 for Lithium Insertion using Anodic TiO_2 Nanotube Arrays. *Nanotechnology* **2009,** *20* (22), 225701.

(51) Liu, D.; Cao, G., Engineering Nanostructured Electrodes and Fabrication of Film Electrodes for Efficient Lithium Ion Intercalation. *Energy Environ. Sci.* **2010**, *3* (9), 1218.

(52) Li, J.; Hu, H.; Qin, F.; Zhang, P.; Zou, L.; Wang, H.; Zhang, K.; Lai, Y., Flower-like $MoSe_2$/C Composite with Expanded (0 0 2) Planes of Few-layer $MoSe_2$ as the Anode for High-Performance Sodium-Ion Batteries. *Chem. Eur. J.* **2017**, *23* (56), 14004-14010.

(53) Zheng, C.; Chen, C.; Chen, L.; Wei, M., A CMK-5-Encapsulated $MoSe_2$ Composite for Rechargeable Lithium-Ion Batteries with Improved Electrochemical Performance. *J. Mater. Chem. A* **2017**, *5* (37), 19632-19638.

(54) Yousaf, M.; Wang, Y.; Chen, Y.; Wang, Z.; Aftab, W.; Mahmood, A.; Wang, W.; Guo, S.; Han, R. P. S., Tunable Free-Standing Core-Shell CNT@$MoSe_2$ Anode for Lithium Storage. *ACS Appl. Mater. Interfaces* **2018**, *10* (17), 14622-14631.

(55) Xu, Y.; Bahmani, F.; Wei, R., Pyrrhotite $Fe_{1-x}S$ Microcubes as a New Anode Material in Potassium-Ion Batteries. *Microsyst. Nanoeng.* **2020**, *6*, 75.

(56) Lu, C.; Li, Z.; Yu, L.; Zhang, L.; Xia, Z.; Jiang, T.; Yin, W.; Dou, S.; Liu, Z.; Sun, J., Nanostructured Bi_2S_3 Encapsulated within Three-Dimensional N-Doped Graphene as Active and Flexible Anodes for Sodium-Ion Batteries. *Nano Res.* **2018**, *11* (9), 4614-4626.

(57) Zhu, H.; Zhang, F.; Li, J.; Tang, Y., Penne-Like MoS_2/Carbon Nanocomposite as Anode for Sodium-Ion-Based Dual-Ion Battery. *Small* **2018**, *14* (13), 1703951.

(58) Ni, J.; Zhao, Y.; Liu, T.; Zheng, H.; Gao, L.; Yan, C.; Li, L., Strongly Coupled Bi_2S_3@CNT Hybrids for Robust Lithium Storage. *Adv. Energy Mater.* **2014**, *4* (16), 1400798.

(59) Li, N.; Sun, L.; Wang, K.; Zhang, J.; Liu, X., Anchoring $MoSe_2$ Nanosheets on N-Doped Carbon Nanotubes as High Performance Anodes for Potassium-Ion Batteries. *Electrochim. Acta* **2020**, *360*, 136983.

(60) Sehrawat, P.; Julien, C.; Islam, S. S., Carbon Nanotubes in Li-Ion Batteries: A review. *Mater. Sci. Eng. B* **2016,** *213*, 12-40.

(61) Liu, X.-M.; Huang, Z. d.; Oh, S. w.; Zhang, B.; Ma, P.-C.; Yuen, M. M. F.; Kim, J.-K., Carbon Nanotube (CNT)-Based Composites as Electrode Material for Rechargeable Li-Ion Batteries: A review. *Compos. Sci. Technol.* **2012**, *72* (2), 121-144.

(62) Xie, D.; Tang, W.; Wang, Y.; Xia, X.; Zhong, Y.; Zhou, D.; Wang, D.; Wang, X.; Tu, J., Facile Fabrication of Integrated Three-Dimensional C-$MoSe_2$/Reduced Graphene Oxide Composite with Enhanced Performance for Sodium Storage. *Nano Res.* **2016**, *9* (6), 1618-1629.

(63) Xu, Y.; Zhang, C.; Zhou, M.; Fu, Q.; Zhao, C.; Wu, M.; Lei, Y., Highly Nitrogen Doped Carbon Nanofibers with Superior Rate Capability and Cyclability for Potassium Ion Batteries. *Nat. Commun.* **2018**, *9*, 1720.

(64) Li, D.; Zhang, Y.; Sun, Q.; Zhang, S.; Wang, Z.; Liang, Z.; Si, P.; Ci, L., Hierarchically Porous Carbon Supported Sn_4P_3 as a Superior Anode Material for Potassium-Ion Batteries. *Energy Storage Mater.* **2019**, *23*, 367-374.

(65) Li, D.; Sun, Q.; Zhang, Y.; Chen, L.; Wang, Z.; Liang, Z.; Si, P.; Ci, L., Surface-Confined SnS_2@C@rGO as High-Performance Anode Materials for Sodium- and Potassium-Ion Batteries. *ChemSusChem* **2019**, *12* (12), 2689-2700.

(66) Zhang, Y.; Tao, H.; Li, T.; Du, S.; Li, J.; Zhang, Y.; Yang, X., Vertically Oxygen-Incorporated MoS_2 Nanosheets Coated on Carbon Fibers for Sodium-Ion Batteries. *ACS Appl. Mater. Interfaces* **2018**, *10* (41), 35206-35215.

(67) Zhou, J.; Liu, Y.; Zhang, S.; Zhou, T.; Guo, Z., Metal Chalcogenides for Potassium Storage. *InfoMat* **2020**, *2* (3), 437-465.

(68) Ali, Z.; Tang, T.; Huang, X.; Wang, Y.; Asif, M.; Hou, Y., Cobalt Selenide Decorated Carbon Spheres for Excellent Cycling Performance of Sodium Ion Batteries. *Energy Storage Mater.* **2018**, *13*, 19-28.

(69) Zhang, Y.; Wang, N.; Xue, P.; Liu, Y.; Tang, B.; Bai, Z.; Dou, S., Co_9S_8@Carbon Nanospheres as High-Performance Anodes for Sodium Ion Battery. *Chem. Eng. J.* **2018**, *343*, 512-519.

SYNOPSIS